

1 Quantifying the seasonal variations and regional transport of PM_{2.5} 2 in the Yangtze River Delta region, China: Characteristics, sources, 3 and health risks

4 Yangzhihao Zhan^a, Min Xie^{a,g}, Wei Zhao^b, Tijian Wang^a, Pulong Chen^c, Jun Tian^d, Kuanguang Zhu^e,
5 Da Gao^f, Shu Li^a, Bingliang Zhuang^a, Mengmeng Li^a, Yi Luo^a, Runqi Zhao^a

6 ^a School of Atmospheric Sciences, Nanjing University, Nanjing 210023, China

7 ^b Nanjing Institute of Environmental Sciences, Ministry of Ecology and Environment of the People's Republic of China,
8 Nanjing 210023, China

9 ^c Net Zero Era (Jiangsu) Environmental Technology Co., Nanjing 210023, China

10 ^d Academy of Environmental Planning and Design. Co.,Ltd., Nanjing University, Nanjing 210023, China

11 ^e Hubei Provincial Academy of Eco-Environmental Sciences, Wuhan 430073, China

12 ^f State Key Joint Laboratory of Environment Simulation and Pollution Control, School of Environment, Tsinghua University,
13 Beijing 100084, China

14 ^g School of Environment, Nanjing Normal University, Nanjing 210023, China

15 *Correspondence to:* Min Xie (minxie@nju.edu.cn), Wei Zhao (zhaowei@nies.org)

16 **Abstract.** Given the increasing complexity of the chemical composition of PM_{2.5}, identifying and quantitatively assessing
17 the contributions of pollution sources has played an important role in formulating policies to control particle pollution. This
18 study provides a comprehensive assessment between PM_{2.5} chemical characteristics, sources, and health risks based on
19 sampling data conducted over one year (March 2018 to February 2019) in Nanjing. Results show that PM_{2.5} exhibits a
20 distinct variation across different seasons, which is primarily driven by emissions, meteorological conditions, and chemical
21 conversion of gaseous pollutants. First, the chemical mass reconstruction shows that secondary inorganic aerosols (SIA,
22 62.5 %) and carbonaceous aerosols (21.3%) contributed most to the PM_{2.5} mass. The increasing oxidation rates of SO₂ and
23 NO₂ from summer to winter indicate that the secondary transformation of gaseous pollutants is strongly positively correlated
24 with relative humidity. Second, the positive matrix factorization (PMF) method shows that identified PM_{2.5} sources include
25 secondary inorganic aerosol sources (SIS, 42.5%), coal combustion (CC, 22.4%), industry source (IS, 17.3%), vehicle
26 emission (VE, 10.7%), fugitive dust (FD, 5.8%) and other sources (1.3%). The Hybrid Single Particle Lagrangian Integrated
27 Trajectory (HYSPLIT) model and the concentration-weighted trajectory (CWT) analysis are used to further explore different
28 spatial distributions and regional transport of sources. The concentrations (10-11 μg·m⁻³) of SIS and CC distribute in
29 Nanjing and central China in winter. The concentrations (8-10 μg·m⁻³) of IS and VE are potentially located north of Jiangsu,
30 Anhui, and Jiangxi. Finally, the health risk assessment indicates that the carcinogenic and non-carcinogenic risks of toxic
31 elements (Cr, As, Ni, Mn, V, and Pb) mainly come from IS, VE, and CC, which are within the tolerance or acceptable level.
32 Although the main source of pollution in Nanjing is SIS at present, we should pay more attention to the health burden of
33 vehicle emissions, coal combustion, and industrial processes.

35 1. Introduction

36 PM_{2.5} is particulate matter with an aerodynamic equivalent diameter less than or equal to 2.5 μm, and one of the most
37 important air pollutants, which can affect air quality (Sharma et al., 2020), atmospheric visibility (Tseng et al., 2019) and
38 ecosystems (Li et al., 2021). PM_{2.5} can directly enter the human body through the respiratory system and lead to increased
39 health risks (Kumar et al., 2019; Sulaymon et al., 2021). PM_{2.5} concentrations in the United States and Europe have begun to
40 decrease since the 1980s, and those in Japan gradually decreased after 2012 (Zhang et al., 2020). In China, the annual
41 average concentration of PM_{2.5} has decreased by 50% with the implementation of the Air Pollution Prevention and Control
42 Action Plan (APPCAP) in 2013. However, annual PM_{2.5} concentrations in most cities are greater than 10 μg·m⁻³, the air
43 quality guideline of the World Health Organization (Song et al., 2017; Zeng et al., 2019; Cheng et al., 2021), and the number
44 of deaths caused by PM_{2.5} exceeds one million per year (Zhu et al., 2020). It indicates that a comprehensive assessment
45 between PM_{2.5} chemical characteristics, sources, and health risks is significant for pollution control measures in the key
46 regions of China.

47 Understanding the chemical composition of PM_{2.5} is important for formulating control strategies. Sulfate, nitrate, and
48 ammonium (SNA) are the major secondary inorganic aerosols, whose chemical conversion occurs in homogeneous and
49 heterogeneous reactions (Fan et al., 2020; Chow et al., 2022). Variations in the form of SO₄²⁻ and NH₃ lead to variations in
50 the acid-base balance of aerosols (Roper et al., 2019). Organic carbon (OC) comprises thousands of organic compounds.
51 Elemental carbon (EC) is stable and mainly derived from primary sources of combustion products (Wu et al., 2020; Zhang et
52 al., 2022). Both NO₃⁻/SO₄²⁻ and OC/EC ratios can be reasonably used to evaluate the contribution of mobile and stationary
53 sources to PM_{2.5} in the atmosphere (Zhan et al., 2021). To identify the sources of PM_{2.5}, receptor modelings have been
54 developed, which include positive matrix factorization (PMF), chemical mass balance (CMB), and principal component
55 analysis (PCA) (Zong et al., 2016; Lv et al., 2020). Recently, the combination of the PMF model and trajectory modeling has
56 proven to be powerful to identify source regions and quantify chemical compositions for a receptor site (Zheng et al., 2019).
57 Air exposure models have been widely used to compare the health outcomes of people exposed to different levels of air
58 pollution (Thurston et al., 2016; Conibear et al., 2018). Long-term exposure to PM_{2.5} is particularly significant for
59 cardiovascular disease mortality (Hayes et al., 2020). Trace metals (Cr, Ni, Mn, V, and Pb) are a minor component of PM_{2.5}
60 in qualitative terms, but the health risk of toxic elements through inhalation of PM_{2.5} exceeds acceptable levels (Jiang et al.,
61 2018; Jeong et al., 2019; Xie et al., 2020). Health risk assessments have been widely used to assess further the non-
62 carcinogenic and carcinogenic health risks of toxic elements in PM_{2.5} (Behrooz et al., 2021; Fang et al., 2021; Li et al., 2022).

63 Chemical characteristics of PM_{2.5} have been widely investigated in the Beijing-Tianjin-Hebei (BTH), the Yangtze River
64 Delta (YRD), and the Pearl River Delta (PRD) during the last decade (Huang et al., 2017; Liu et al., 2017; Li et al., 2020). In
65 the megacity of China, the occurrence of haze may be exacerbated by interactions between aerosols and meteorological
66 conditions and regional transport (Zeng et al., 2019; Fan et al., 2020; Wang et al., 2023). The YRD region is China's
67 scientific research base and comprehensive transportation hub. The annual PM_{2.5} concentration in the YRD has been reduced

68 by 45.6% from 2016 to 2018. However, as a mega-city in the YRD, the PM_{2.5} in Nanjing still exceeds the National Ambient
69 Air Quality Standard (35 µg·m⁻³ as an annual average) by more than 38 % (Nie et al., 2018). Source apportionment studies
70 mainly focus on the relative importance of local emission and regional transportation on PM_{2.5} at a specific site using the
71 PMF model and the backward trajectory analysis (Zheng et al., 2019; Yan et al., 2021; Lv et al., 2022). Some studies
72 involved the health risks of toxic elements in PM_{2.5} (Zhang et al., 2019; Fang et al., 2021), and only a few studies discussed
73 the classification of toxic elements according to PMF results (Wang et al., 2019; Wang et al., 2020). However, there were
74 two shortcomings in previous studies: (1) Given the uneven geographical distribution of observation sites and difficulties in
75 data collection, most studies were based on short-term data comparisons and lacked systematic comparisons of the
76 distinctive seasonality, regional transport, and meteorological effects of various elements and sources. (2) A comprehensive
77 assessment of the health risks of toxic elements in each source of PM_{2.5} was still scarce, which limited the implementation of
78 long-term pollution control measures in megacities.

79 In this work, we provide high-quality composition data for PM_{2.5} in the typical YRD city, including their chemical
80 characteristics and diurnal variations. Besides, the measured PM_{2.5} in its entirety is successfully apportioned to various
81 contributing sources by PMF and CWT methods. Finally, potential risks associated with exposure to airborne toxic elements
82 are identified based on the health risk assessment. The results can systematically assess the relationship between chemical
83 characteristics, sources, and health risks of PM_{2.5}, and serve to guide PM_{2.5} control measures for other megacities.

84

85 **2. Data and Methodology**

86 **2.1 Chemical component sampling, air quality and meteorological data**

87 Hourly concentrations of particulate matter (PM) components from December 2018 to February 2019 in Nanjing were
88 used in this study. The elemental carbon (EC), organic carbon (OC), 30 trace elements (Si, Al, As, Ca, K, Co, Mo, Ag, Sc, Tl,
89 Pd, Br, Te, Ga, Cs, Pb, Se, Hg, Cr, Cd, Zn, Cu, Ni, Fe, Mn, Ti, Sb, Sn, and V), and 8 soluble components in aerosols (Na⁺,
90 K⁺, Mg²⁺, Ca²⁺, Cl⁻, NO₃⁻, SO₄²⁻, and NH₄⁺) were quantified in each PM_{2.5} sample. PM_{2.5} samples were collected on the
91 rooftop of the School of Atmospheric Sciences, Xianlin Campus, Nanjing University (32.12 °N, 118.96 °E). OC and EC
92 were analyzed by the online carbon fraction Monitor (EA-32, Everisetech Co., Beijing). OC and EC were separated by step
93 heating and then determined by the non-dispersive infrared method. The components of heavy metals were collected by the
94 atmospheric heavy metal Monitor (AMS-100, Fpigroup Co., Hangzhou). The volumetric concentration of heavy elements
95 (ng·m⁻³) was obtained by detecting the concentration of PM enriched on the filter membrane using the β ray absorption
96 principle (Wang et al., 2020). The soluble components sampling instrument was the In-situ Gas and Aerosol Compositions
97 Monitor (IGAC, Fortelice International Co., Taiwan). It consisted of the wet concentric circular tube, the gas gel processor,
98 and the ion chromatograph. The sampling inlet was about 20 m above the ground and the flow rate was 16.67 L·min⁻¹. The
99 collected liquid samples were filtered by defoaming and then injected into the ion chromatography analyzers to analyze the

100 ion components from the gases and the aerosols. The detection limits were below $0.12 \mu\text{g}\cdot\text{m}^{-3}$ and the collection efficiency
101 was higher than 90% (Zhan et al., 2021).

102 Air pollutants, including $\text{PM}_{2.5}$, PM_{10} , O_3 , NO_2 , SO_2 , and CO , were monitored by the National Environmental
103 Monitoring Center (NEMC) of China. These data were issued hourly on the national urban air quality real-time publishing
104 platform (<https://air.cnemc.cn:18007/>, last access: 7 April 2023). Meteorological parameters included air pressure, air
105 temperature, relative humidity, wind speed, and boundary layer height. We collected hourly data from the National Climatic
106 Data Center (NCDC) of the University of Wyoming website (<http://weather.uwyo.edu/surface/>, last access: 7 April 2023).
107 Regarding boundary layer height, daily sounding vertical profiles were extracted from the national benchmark climate
108 Nanjing station 58238 (32.00°N , 118.48°E) and were also acquired from this website. The quality assurance and quality
109 control (QA/QC) procedures were used at each site according to the method of Xie et al. (2016) and Gao et al. (2021). $\text{PM}_{2.5}$
110 component data were collected hourly, and the study was based on high-time resolution data. We measured 10% of all
111 samples as parallel sampling and the pass rate was over 95%. We defined the missing sampling of atmospheric pollutant data
112 as -999 to facilitate PMF processing. The chemical mass reconstruction method was used to correct potential measurement
113 errors, which was described in detail in Section 2.2. The QA/QC procedures have passed the artificial random inspection of
114 extreme value and time consistency.

115 2.2 Mass and chemical composition determination for $\text{PM}_{2.5}$

116 Due to the limitation in sampling location and equipment, the sum of measured species was often lower than the
117 gravimetric mass. Chemical mass reconstruction (CMR) attempted to achieve closure between the gravitational mass and the
118 sum of components and correct potential measurement errors. In this study, the reconstructed result and the gravimetric
119 result exhibited a significant correlation, with a mean R^2 of 0.93, indicating that the chemical reconstruction method had
120 strong reliability. Following the work of Xu et al. (2021), eight categories of chemical components in chemically
121 reconstructed $\text{PM}_{2.5}$ can be expressed as follows:

$$122 \quad \text{PM}_{2.5} = \text{OM} + \text{EC} + \text{MD} + \text{TM} + \text{SO}_4^{2-} + \text{NO}_3^- + \text{NH}_4^+ + \text{Cl}^- \quad (1)$$

123 where OM refers to the organic matter. The OC to OM conversion coefficient at urban sites is 1.6 (Brokamp et al., 2017).
124 The calculation of mineral dust (MD) is based on crustal element oxides (Yan et al., 2020):

$$125 \quad \text{MD} = 2.14 \times \text{Si} + 1.67 \times \text{Ti} + 1.89 \times \text{Al} + 1.40 \times \text{Ca} + 1.58 \times \text{Mn} + 1.43 \times \text{Fe} + 1.21 \times \text{K} + 1.67 \times \text{Mg} \quad (2)$$

126 where Si is estimated as multiplying Al in crustal material by a converting factor (3.14) (Zheng et al., 2019). Trace metals
127 (TM) represent the sum of 30 different types of heavy metals:

$$128 \quad \begin{aligned} \text{TM} = & \text{As} + \text{Co} + \text{Mo} + \text{Ag} + \text{Sc} + \text{Tl} + \text{Pd} + \text{Br} + \text{Te} + \text{Ga} + \text{Cs} + \text{Pb} \\ & + \text{Se} + \text{Hg} + \text{Cr} + \text{Cd} + \text{Zn} + \text{Cu} + \text{Ni} + \text{Sb} + \text{Sn} + \text{V} + \text{Ba} \end{aligned} \quad (3)$$

129 2.3 Identification of source by the positive matrix factorization (PMF) model

130 The positive matrix factorization (PMF) was developed by the Environmental Protection Agency (EPA) and has been
131 widely adopted to classify $\text{PM}_{2.5}$ into different factors (Zong et al., 2016). The US EPA PMF version 5.0 was referred to in

132 this study. The basic principle of the PMF model was to calculate the weight error of each chemical component in the
133 particulate matter and then determined its main pollution source and contribution rate by the least square method (Paatero
134 and Tapper, 1994). The equation of the PMF model can be expressed as follow:

$$135 \quad X_{ij} = \sum_{k=1}^p g_{ik} f_{kj} + e_{ij} \quad (4)$$

136 where X_{ij} is the concentration of the ij th sample; g_{ik} represents the contribution of the ik th sample; f_{kj} represents the
137 mass fraction of the jk th and e_{ij} is the residual between the measured mass concentration of the ij th sample and its analytical
138 value. The purpose of the PMF model is to find the minimum Q value with the concentration file and uncertainty file (u_{ij})
139 introduced into the model. The objective function Q is defined as follows:

$$140 \quad Q_{ij} = \sum_{i=1}^n \sum_{j=1}^m \left[\frac{X_{ij} - \sum_{k=1}^p g_{ik} f_{kj}}{u_{ij}} \right]^2 \quad (5)$$

141 where Q is the sum of all sample residuals and their uncertainties u. In this study, the fitting species included 41 types of
142 chemical species of PM_{2.5} that were selected and validated to ensure that the value of the objective function Q was
143 minimized.

$$144 \quad Unc = \frac{5}{6} \times MDL \quad (6)$$

$$145 \quad Unc = \sqrt{(Error\ Fraction \times concentration)^2 + (0.5 \times MDL)^2} \quad (7)$$

146 where Unc is the uncertainty. MDL is the method detection limi. If the concentration is less than or equal to the MDL
147 provided, Unc is calculated using a fixed fraction of the MDL (Taylor et al., 2020). If the concentration is greater than the
148 MDL, the calculation is based on the concentration fraction and MDL.

149 First, we excluded more than 50% of the dataset for species below the method detection limit (MDL) and retained 23
150 species that were significantly correlated with PM_{2.5}. Second, we calculated the uncertainty (Unc) for each species based on
151 the concentration fraction and MDL (Taylor et al., 2020). Third, different numbers of factors were tested with random seeds
152 in 20 iterations of each run. When the number of factors was set to six, the fitting degree of the model calculation results was
153 the highest, with a correlation coefficient of 0.93, and the species almost showed a normal curve. Finally, the bootstrap (BS)
154 and displacement (DISP), and BS-DISP diagnostic analysis were also used to evaluate the rationality of the apportioned
155 factor profiles and contributions. BS is used to detect and estimate the disproportionate effects of a small set of observations
156 on the solution and also, to a lesser extent, the effects of rotational ambiguity. The value of the F-peak strength was ensured

157 to be 0.5 to eliminate the rotation ambiguity. The mapping for each factor in this study was more than 80% from the BS run,
158 indicating the six-factor solution was appropriate.

159 **2.4 Source apportionment by backward trajectory calculation and CWT analysis**

160 The Hybrid Single Particle Lagrangian Integrated Trajectory (HYSPLIT) model was developed by the National
161 Oceanic and Atmospheric Administration (NOAA) and the Bureau of Meteorology Australia to simulate and analyze the
162 movement, deposition, and diffusion of airflow. The reanalysis data with a spatial resolution of one degree and a temporal
163 resolution of 6 h (00:00, 06:00, 12:00, and 18:00 UTC) were obtained from the Global Data Assimilation System (GDAS)
164 (<https://rda.ucar.edu/datasets/>, last access: 7 April 2023). To locate the potential source areas for the corresponding
165 components, we used the HYSPLIT model to analyze the backward trajectory of airflow from March 2018 to February 2019.
166 48-hour backward trajectories terminated at a height of 100 m above ground level were calculated at the starting point
167 (32.07 °N, 118.78 °E). Due to the high uncertainty of a single backward trajectory, we drew multiple trajectories and
168 performed cluster analysis. The cluster analysis was a multivariate statistical technique using the Angle Distance algorithm,
169 which could quantify the relationship among the pollution concentrations in each source area (Shu et al., 2017).

170 The concentration-weighted trajectory (CWT) analysis was further used to determine the relative contribution of
171 different areas. The CWT analysis was conducted by the TrajStat software, which was a GIS (geographic information system)
172 application that enabled the user to visualize and analyze the spatial and meteorological data with multiple data formats
173 (Feng et al., 2021). In this study, the meteorological data used for the HYSPLIT model and the CWT method remained the
174 same. The CWT method divided the research area into small equal grids, set a standard value for the research object, and
175 defined the trajectory exceeding the standard value as the pollution trajectory. According to the criteria of the Chinese
176 National Ambient Air Quality Standards (NAAQS), the standard value of the PM_{2.5} concentrations was 75 µg·m⁻³ in this
177 study. The spatial resolution was 0.5×0.5 (Liu et al., 2018). The CWT method reflected the pollution degree of different
178 trajectories by calculating the weight concentration of the airflow trajectory in potential source areas:

$$179 \quad C_{ij} = \frac{1}{\sum_{i=1}^M \tau_{ijl}} \sum_{l=1}^M C_l \tau_{ijl} \quad (8)$$

180 where C_{ij} is the average weight concentration of grid ij , C_l is the pollutant concentration based on trajectory l that passes
181 through grid ij , and τ_{ij} is the residence time of trajectory l in grid ij . Similarly, to reduce the uncertainty caused by the
182 smaller n_{ij} , the CWT value is multiplied by the weight function as well (Wong et al., 2022):

$$183 \quad W_{ij} = \begin{cases} 1.00 & (80 < n_{ij}) \\ 0.72 & (20 < n_{ij} \leq 80) \\ 0.42 & (10 < n_{ij} \leq 20) \\ 0.05 & (n_{ij} \leq 100) \end{cases} \quad (9)$$

184 where n_{ij} is the number of trajectories that pass through the ij^{th} cell. W_{ij} is an empirical weight function to reduce the undue
 185 influence of small n_{ij} on the CWT values (Fan et al., 2019). In this study, the CWT value of each identified source derived
 186 from the PMF model was calculated.

187 2.5 Health risk assessment

188 The human health risk from heavy metals in PM_{2.5} may occur through exposure to ambient air (Zhang et al., 2019).
 189 Based on the PMF analysis, we selected six toxic elements (Cr, As, Ni, Mn, V, and Pb) for the exposure risk assessment. Cr,
 190 Ni and As have both carcinogenic and non-carcinogenic effects, Mn and V mainly have non-carcinogenic effects, and Pb
 191 mainly produces a carcinogenic effect (Jiang et al., 2018). The non-carcinogenic and carcinogenic risks from the toxic
 192 species of PM_{2.5} were evaluated by the hazard quotient (HQ) and lifetime carcinogenic risk (LCR), respectively. The US
 193 EPA human health risk assessment models were used to conduct carcinogenic and non-carcinogenic risk assessments (Khan
 194 et al., 2016):

$$195 \quad EC_{inh} = \frac{GA \times ET \times EF \times ED}{AT} \quad (10)$$

$$196 \quad HQ = \frac{EC_{inh}}{RfC_i \times 1000 \mu\text{g} \cdot \text{mg}^{-1}} \quad (11)$$

$$197 \quad LCR = IUR \times EC_{inh} \quad (12)$$

198 where EC_{inh} is the average daily exposure concentration of toxic elements inhaled through respiration. GA is the
 199 concentration of toxic elements in each source composition. ET is the exposure time, 24 h·d⁻¹; EF is the exposure frequency,
 200 365 d·yr⁻¹; ED is the exposure duration, 30 yr; and AT is the average exposure time, calculated by $ED \text{ yr} \times 365 \text{ d} \cdot \text{yr}^{-1} \times 24$
 201 $\text{h} \cdot \text{d}^{-1}$ for non-carcinogens and $70 \text{ yr} \times 365 \text{ d} \cdot \text{yr}^{-1} \times 24 \text{ h} \cdot \text{d}^{-1}$ for carcinogens. RfC_i is the inhalation reference concentration
 202 ($\text{mg} \cdot \text{m}^{-3}$). IUR is the inhalation unit risk ($(\mu\text{g} \cdot \text{m}^{-3})^{-1}$). HQ greater than 1 indicated a non-carcinogenic risk to human health.
 203 For carcinogenic risk, $LCR < 10^{-6}$ means no cancer risk, LCR between 10^{-6} and 10^{-4} is acceptable or tolerable, and $LCR > 10^{-4}$
 204 is intolerable. The exposure parameters were shown in Table 1 (Jiang et al., 2018; Zhang et al., 2019).

205
 206
 207

208 **Table 1. Exposure parameters of toxic elements through inhalation route in health risk assessments.**

Toxic elements	RfC _i ($\mu\text{g}\cdot\text{m}^{-3}$) ⁻¹	IUR ($\text{mg}\cdot\text{m}^{-3}$)
Cr	1.0×10^{-4}	1.2×10^{-2}
As	1.5×10^{-5}	4.3×10^{-3}
Ni	1.4×10^{-5}	2.4×10^{-4}
Mn	5.0×10^{-5}	—
V	1.0×10^{-4}	—
Pb	—	1.2×10^{-5}

209

210 **3. Results and discussions**211 **3.1 Chemical components, meteorological parameters and diurnal variations**

212 Table 2 shows the seasonal average of chemical components and meteorological parameters from March 2018 to
 213 February 2019. In this study, March to May 2018 is defined as spring, June to August 2018 is defined as summer, September
 214 to November 2018 is defined as fall, and December 2018 to February 2019 is defined as winter. The daily average
 215 concentration of PM_{2.5} ranged from 6.7 to 234.0 $\mu\text{g}\cdot\text{m}^{-3}$, with an annual average of 68.7 $\mu\text{g}\cdot\text{m}^{-3}$. The order of average
 216 concentrations of PM_{2.5} in each season was winter ($113.9 \mu\text{g}\cdot\text{m}^{-3}$) > spring ($99.1 \mu\text{g}\cdot\text{m}^{-3}$) > autumn ($38.9 \mu\text{g}\cdot\text{m}^{-3}$) > summer
 217 ($23.7 \mu\text{g}\cdot\text{m}^{-3}$). Seasonal variations of PM_{2.5} were closely related to emission and meteorological conditions. In spring, the
 218 wind speed (WS) was higher ($3.5 \text{ m}\cdot\text{s}^{-1}$) than those in other seasons. Pearson correlation showed that PM_{2.5} concentrations
 219 were significantly ($p<0.01$) correlated to WS ($r=-0.36$) in spring. In summer, high boundary layer height (BLH) (520.4m)
 220 significantly reduced PM_{2.5} concentrations. In autumn and winter, PM_{2.5} showed significant correlations between
 221 temperature ($r=-0.53$), relative humidity ($r=0.62$) and BLH ($r=-0.43$). Biomass emissions in most cities and industrial
 222 emissions in industrial cities contribute 7-27% to PM_{2.5} mass in applicable cities (Tao et al., 2017). Coal consumption and
 223 population density have a significantly positive effect on PM_{2.5} concentration (Zhou et al., 2018; Chow et al., 2022). The
 224 highest level of PM_{2.5} in winter was due to coal consumption, lower temperatures (4.9°C), higher humidity (79.6%), and
 225 lower BLH (419.7m) than in summer.

226 The seasonal variation of anthropogenic emissions also considerably affected PM_{2.5} concentrations. The order of the
 227 major components in PM_{2.5} was NO_3^- (20-31%) > SO_4^{2-} (16-27%) > NH_4^+ (11-19%) > mineral dust (8-14%) > OM (6-
 228 14%) > EC (2-4%) > trace metals (2-3%) > Cl⁻ (1-3%). Sulfate, nitrate, and ammonium (SNA) accounted for 60% of the
 229 total PM_{2.5} and were closely related to the secondary transformation of gaseous precursors. The concentration ratio of NO_3^-
 230 to SO_4^{2-} ($\text{NO}_3^-/\text{SO}_4^{2-}$) was used to differentiate the relative importance of nitrogen (generally related to vehicle emissions)
 231 and sulfur (normally related to stationary sources) in the atmosphere (Liu et al., 2019). Over the past few years, the mass
 232 ratio of $\text{NO}_3^-/\text{SO}_4^{2-}$ was 2.13 in Ningbo, 1.89 in Hangzhou, and 1.21 in Beijing (Huang et al., 2017; Li et al., 2018). In this
 233 study, the average ratios of $\text{NO}_3^-/\text{SO}_4^{2-}$ were 1.81 in spring, 1.20 in summer, 2.34 in autumn, and 1.59 in winter, respectively,
 234 indicating the enhanced secondary transformation of gaseous pollutants (e.g. SO₂, NO_x, VOCs) during heavily polluted

235 periods (Liu et al., 2016; Liu et al., 2018). The oxidation rates of SO₂ and NO₂ need to be further investigated.
 236 Carbonaceous aerosols (OM and EC) accounted for 12% and 14% of PM_{2.5} in spring and winter, respectively. The large
 237 increase in the number of coal fires used for residential heating in winter may increase the abundance of carbon-containing
 238 emissions, including OC, EC, and VOC_s (Islam et al., 2020). Compared with 2015, the concentrations of OM and EC
 239 decreased from 22.9% to 12.8% (Chen et al., 2017). This may be related to policies to control coal combustion and motor
 240 vehicle emissions, considering similar meteorological conditions in the two periods (Tao et al., 2017; Jeong et al., 2019).

241

242 **Table 2. Seasonal average concentration of components of PM_{2.5}, in $\mu\text{g}\cdot\text{m}^{-3}$ and % in brackets, and meteorological parameters. T,**
 243 **RH, WS, and BLH represent air temperature, relative humidity, wind speed and boundary layer height, respectively.**

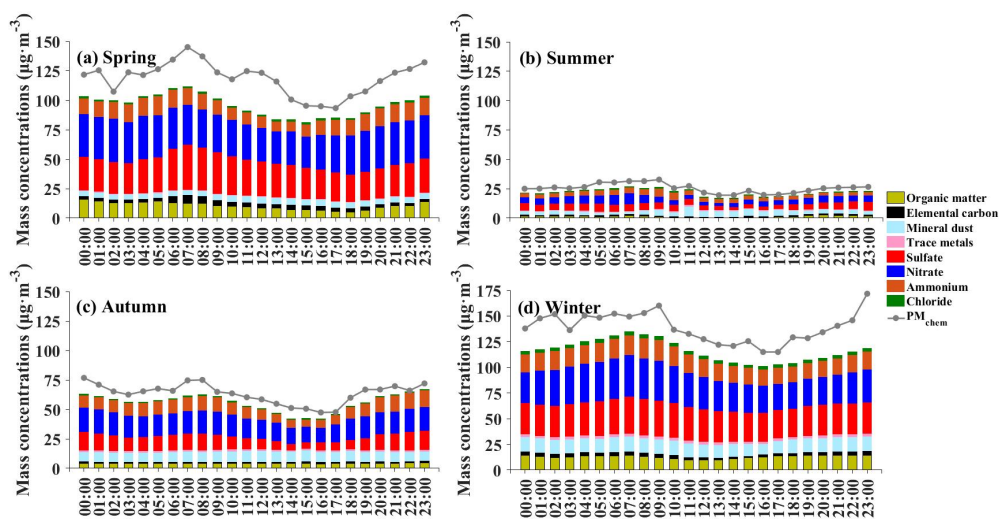
Components and meteorological parameters	Spring	Summer	Autumn	Winter
PM _{2.5}	99.1	23.7	38.9	113.9
SO ₄ ²⁻	20.5 (20.7)	5.2 (21.9)	7.3 (18.8)	31.5 (27.7)
NO ₃ ⁻	16.9 (17.1)	5.3 (22.4)	9.8 (25.2)	27.2 (23.9)
NH ₄ ⁺	15.1 (15.2)	3.2 (13.5)	7.1 (18.3)	11.5 (10.1)
OM	11.7 (11.8)	1.6 (6.8)	4.1 (10.5)	11.0 (9.7)
EC	2.3 (2.3)	0.8 (3.4)	1.6 (4.1)	3.6 (3.2)
Mineral dust	13.2 (13.3)	2.3 (9.7)	2.7 (6.9)	8.7 (7.6)
Trace metals	2.7 (2.7)	0.5 (2.1)	0.5 (1.3)	1.6 (1.4)
Cl ⁻	2.7 (2.7)	1.6 (6.8)	0.8 (2.1)	1.7 (1.5)
T (°C)	18.8	27.6	19.4	4.9
RH (%)	86.5	58.2	73.1	79.6
WS (m·s ⁻¹)	3.5	2.9	2.7	2.1
BLH (m)	469.7	520.4	443.6	419.7

244

245 Figure 1 shows the diurnal variation of chemical components in PM_{2.5}. The seasonal differences were mainly reflected
 246 in the variation in the timing of peak values. In spring (Fig. 1a), the highest and lowest PM_{2.5} concentrations were 143.6
 247 $\mu\text{g}\cdot\text{m}^{-3}$ at 7:00 and 94.8 $\mu\text{g}\cdot\text{m}^{-3}$ at 14:00, respectively. The concentration of SNA had obvious diurnal variations. From 6:00
 248 to 18:00, the average concentration of NO₃⁻ increased from 17.6 to 21.8 $\mu\text{g}\cdot\text{m}^{-3}$, while the average concentration of SO₄²⁻
 249 decreased from 23.2 to 15.9 $\mu\text{g}\cdot\text{m}^{-3}$. In summer (Fig. 1b), the highest and lowest PM_{2.5} concentrations were 23.5 $\mu\text{g}\cdot\text{m}^{-3}$ at
 250 9:00 and 14.2 $\mu\text{g}\cdot\text{m}^{-3}$ at 14:00, respectively. The maximum concentration difference of SNA between day and night was less
 251 than 10 $\mu\text{g}\cdot\text{m}^{-3}$, indicating the study area was in a relatively stable background field (Chen et al., 2018). In autumn (Fig. 1c),
 252 the highest and lowest PM_{2.5} concentrations were 77.1 $\mu\text{g}\cdot\text{m}^{-3}$ at 8:00 and 47.8 $\mu\text{g}\cdot\text{m}^{-3}$ at 16:00, respectively. The
 253 concentration of SNA increased at night and decreased during the day. The maximum concentration difference was more

254 than $20 \mu\text{g}\cdot\text{m}^{-3}$. In winter (Fig. 1d), from 18:00 to 23:00, the concentration of SNA increased from $74.5 \mu\text{g}\cdot\text{m}^{-3}$ to 108.7
 255 $\mu\text{g}\cdot\text{m}^{-3}$, with increasing rates of $8.5 \mu\text{g}\cdot\text{m}^{-3}\cdot\text{h}^{-1}$. The height of the atmospheric boundary layer decreased early in the winter
 256 afternoons (Chen et al., 2018). The values of $\text{PM}_{2.5}$ in winter were higher at night due to the coal combustion and biomass
 257 burning (BB) for residential heating (Zou et al., 2017). In summary, compared with the spring and winter, $\text{PM}_{2.5}$ presented
 258 similar and relatively flat diurnal patterns in both autumn and summer. Although the seasonal variations of mass
 259 concentrations and aerosol compositions were substantially different, the concentrations of aerosol species showed similar
 260 diurnal variation patterns during all the sampling days with higher values in the nighttime and early morning, suggesting that
 261 the factors driving the diurnal variations were similar.

262



263

264 **Figure 1. Average diurnal variation of the concentrations of major chemical components of $\text{PM}_{2.5}$ per each season.**

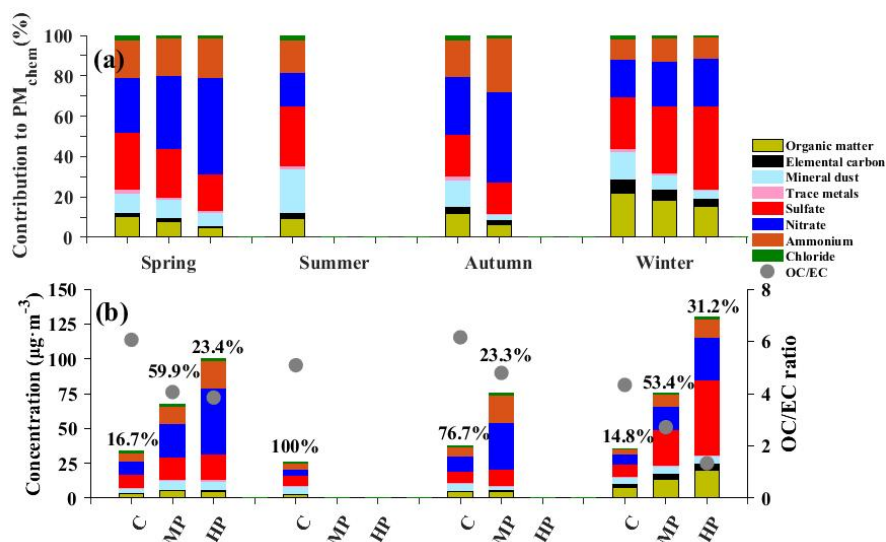
265

266 3.2 Variation of $\text{PM}_{2.5}$ chemical compositions at different pollution levels

267 Figure 2 presents the $\text{PM}_{2.5}$ concentrations and components at different pollution levels. In this study, it was defined as
 268 the clean day (C) when the daily average $\text{PM}_{2.5}$ concentrations were less than $35 \mu\text{g}\cdot\text{m}^{-3}$, the moderate pollution day (MP)
 269 when $\text{PM}_{2.5}$ concentrations were more than $35 \mu\text{g}\cdot\text{m}^{-3}$ and less than $150 \mu\text{g}\cdot\text{m}^{-3}$, and the heavy pollution day (HP) when
 270 $\text{PM}_{2.5}$ concentrations were more than or equal to $150 \mu\text{g}\cdot\text{m}^{-3}$. As shown in Figure 2a, the annual average concentration of the
 271 water-soluble inorganic ions (WSIIs) was $41.9 \mu\text{g}\cdot\text{m}^{-3}$, and accounted for 61.8% of $\text{PM}_{2.5}$. WSIIs were largely responsible for
 272 the variability in $\text{PM}_{2.5}$. The ratios of SNA in spring and winter were similar, with ratios of 65.0% for clean days, 75.0% for
 273 moderate pollution days, and 83.9% for heavy pollution days. With the degradation of air quality, the contribution of NO_3^-
 274 noticeably increased from 27.5% to 47.8% in spring and from 28.9% to 44.7% in autumn. To understand the oxidation rates
 275 of SO_2 and NO_2 , the sulfur oxidation rate and nitrogen oxidation rate (defined as $\text{SOR} = \text{SO}_4^{2-}/(\text{SO}_4^{2-} + \text{SO}_2)$ and $\text{NOR} =$
 276 $\text{NO}_3^-/(\text{NO}_3^- + \text{NO}_2)$) were calculated. The critical value of SOR and NOR in the atmosphere are both 0.1 (Win et al., 2020).

277 The order of the seasonal average NOR was winter (0.21) > spring (0.18) > autumn (0.17) > summer (0.15), while the order
278 of the seasonal average SOR was winter (0.51) > spring (0.43) > autumn (0.42) > summer (0.36). PM_{2.5} pollution in winter is
279 associated with high RH and rapid production of particulate sulfate from the oxidation of SO₂ emitted by coal combustion
280 (Wang et al., 2020). From summer to winter, the NOR and SOR values increased by 40.0% and 41.6%, respectively. SOR
281 and NOR showed a strong positive correlation with relative humidity, with a correlation coefficient of 0.53 and 0.61,
282 respectively. The contribution of coal combustion varied between 30 and 57% of PM_{2.5} in winter (Zhang et al., 2017). Under
283 the conditions of high coal combustion emissions and high RH, the rapid oxidation of SO₂ occurred to produce sulfate. The
284 sensitivity of PM_{2.5} to surface temperature, wind speed, and boundary layer height is negative, while the sensitivity to
285 relative humidity is positive (Chen et al., 2018; Sulaymon et al., 2021). In summer, the correlation coefficients of PM_{2.5} with
286 RH, T, WS, and BLH were 0.42, -0.47, -0.15, and -0.23, respectively. In winter, the correlation coefficients of PM_{2.5}
287 concentration with RH, T, WS, and BLH were 0.74, -0.57, -0.31, and -0.32, respectively. High RH (79.6%), low temperature
288 (4.9°C), low WS (2.1m·s⁻¹), and low BLH (419.7m) provided favorable conditions for the accumulation of PM_{2.5}.

289 Coal combustion, biomass burning, and motor vehicle emissions all lead to a remarkable increase in carbonaceous
290 aerosols (Chow et al., 2022). As shown in Figure 2b, carbonaceous species also had a significantly enhanced contribution in
291 the colder season compared to the warmer season. The seasonal differences might be related to the effects of meteorological
292 conditions and source emissions. Pearson correlation showed that the relationships between OM and EC and meteorological
293 parameters (T, RH, WS, and BLH) were not significant (Table 2). To explore the possible pollution sources, it is feasible to
294 study the mass ratio of OC/EC under different pollution levels. OC comprises thousands of organic compounds. EC is stable
295 and mainly derived from primary sources of combustion products (Zhang et al., 2017; Wu et al., 2020). The OC/EC mass
296 ratio of motor vehicle emissions (1.1) is lower than that of coal combustion (2.7) and biomass burning (9.0) (Xu et al., 2021).
297 In this study, the OC/EC ratios continuously decreased as air pollution got worse, and the values ranged from 6.1 (C), 4.1
298 (MP) to 3.9 (HP) in spring, from 6.2 (C) to 4.8 (MP) in autumn and from 4.3 (C), 2.7 (MP) to 1.3 (HP) in winter. The annual
299 average ratio of OC/EC decreased by 56.1% from clean days to heavy pollution days. If the OC/EC values were in the range
300 of 2.5-5.0, vehicle exhaust emissions were considered as the main source of OC and EC in aerosols, whereas if the OC/EC
301 values were in the range of 5.0-10.5, coal combustion was considered the main source of OC and EC in aerosols (Gao et al.,
302 2018; Liu et al., 2018). Distinct differences in the evolution of the OC/EC ratio on polluted days imply that mobile sources
303 are likely more important. Both the increase in motor vehicle emissions and the formation of meteorological conditions
304 conducive to pollutant accumulation contribute to the decrease in the OC/EC ratio



305
 306 **Figure 2. Chemical compositions of PM_{2.5} and mass ratio of OC/EC at different pollution levels of the total samples per season. C,**
 307 **MP, and HP represent the clean day, moderately polluted day, and heavily polluted day, respectively. “%” represents the**
 308 **proportion of the filter sample quantity at each pollution level out of the total samples.**

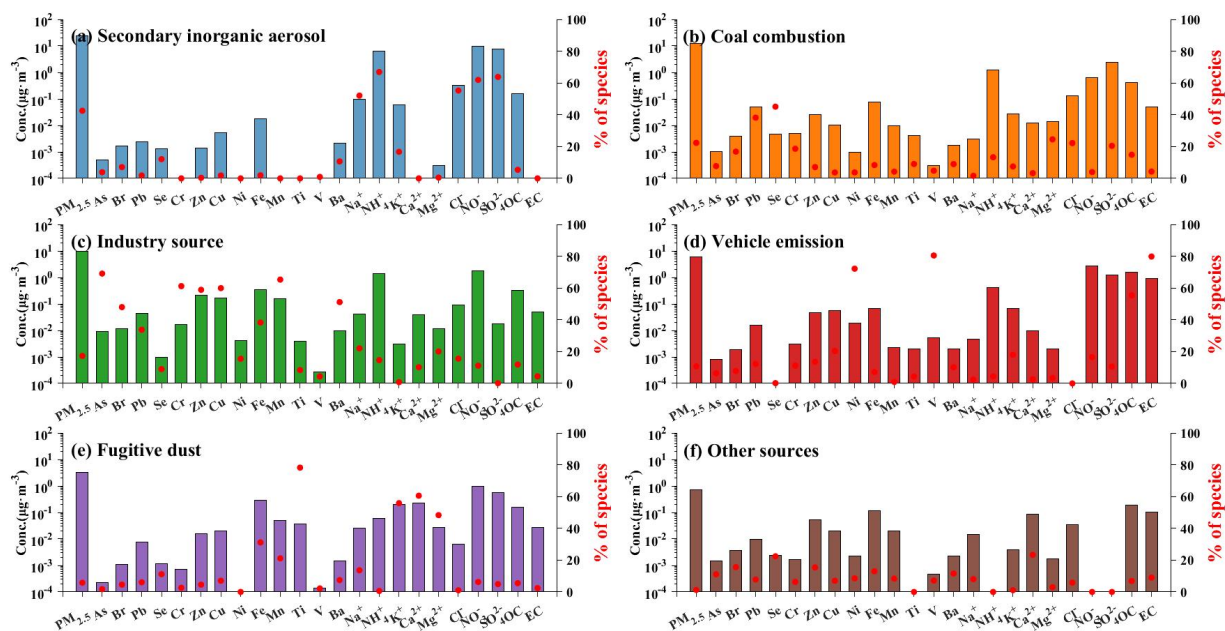
309

310 3.3 Source identification and apportionment

311 3.3.1 Elemental profile and source apportionment from the PMF model

312 To further quantitatively determine the source apportionment of PM_{2.5}, the EPA PMF5.0 model was adopted. The
 313 number of factors in the PMF model corresponded to the number of sources of PM_{2.5} in this study. When the number of
 314 factors was set to six, the fitting degree of the model calculation results was the highest. Figure 3 presents the factor profiles
 315 and relative contributions of six factors to each species (% of species total), including secondary inorganic aerosol source
 316 (SIS), coal combustion (CC), industry source (IS), vehicle emission (VE), fugitive dust (FD), and other sources (OS). The
 317 meaning of % is the proportion of each chemical component in each source of PM_{2.5}. As shown in Figure 3a, the
 318 compositions of SIS were more clear than other sources. NO₃⁻ and SO₄²⁻ are mainly from the oxidation of NO_x and SO₂,
 319 while NH₄⁺ probably comes from the conversion processes between ammonia and sulfuric and nitric acid (Win et al., 2020).
 320 Factor 1 was identified as the SIS with distinctly high loads of NH₄⁺ (66.9%), NO₃⁻ (61.9%), SO₄²⁻ (63.8%) and Cl⁻ (55.3%).
 321 In Figure 3b, the high proportion of Pb (38.2%) and Se (45.1%) was identified in Factor 2, associating with moderate
 322 weighting on As (14.3%), SO₄²⁻ (20.5%), and Cl⁻ (22.2%). Pb and As are important identifying elements of coal combustion
 323 and are used as tracers (Xie et al., 2020). SO₄²⁻ is formed by the photochemical oxidation of sulfur-containing precursors
 324 (SO₂ and H₂S) released by coal combustion (Zong et al., 2016). Given the source profile, Factor 2 was related to coal
 325 combustion emissions. Factor 3 (Figure 3c) was characterized by the association of heavy metal pollutants such as As
 326 (42.8%), Pb (33.8%), Cr (61.1%), Zn (58.9%), Cu (59.4%), Fe (38.3%), and Mn (40.1%). As, Pb, Cr, Fe and Mn are related
 327 to metal smelting and processing (Fang et al., 2021). However, the percentage of OC was only 11.3%, while rates of Zn

328 (58.9%) and Cu (59.4%) were higher in Factor 3 (Fig. 3c). Cu, Zn, and OC are used as tracers of a mixed source of traffic
 329 and industrial, and OC is the major pollutant in the vehicle exhaust (Wang et al., 2020). Compared to motor vehicle
 330 emissions, Factor 3 should be significantly influenced by industrial activities. Cu and Zn were mainly from industrial process
 331 sources. As discussed above, Factor 3 was attributed to the IS. Factor 4 (Figure 3d) was characterized by the association of
 332 vehicle emissions, with the high proportions of Ni (54.7%), V (80.5%), OC (55.4%), EC (79.8%), and NO_3^- (20.3%). VOCs
 333 and NO_x released from vehicles were the precursors of the secondary organic compounds and nitrate in $\text{PM}_{2.5}$ and were
 334 important catalysts for increased atmospheric oxidation (Guevara et al., 2021). OC and EC are mainly from the vehicle
 335 exhaust, and Ni and V are usually tracers of heavy oil combustion (Wu et al., 2020; Veld., 2021). Factor 4 contained a high
 336 proportion of OC, EC, and NO_3^- , which could be considered as vehicle emission, while factor 4 contained Ni and V, which
 337 were also influenced by shipping emissions (Gao et al., 2018; Veld., 2021). As shown in Figure 3e, Factor 5 had relatively
 338 high proportions of Fe (31.1%), Ti (78.2%), K^+ (55.8%), Ca^{2+} (60.5%), and Mg^{2+} (48.3%). Ti, Fe, and Mg are both common
 339 crustal elements that can represent the source of mineral dust. K^+ and Ca^{2+} are considered to be significant tracers of biomass
 340 burning, which have obvious seasonal variations (Tong et al., 2020; Silva et al., 2022). Factor 5 was classified as the fugitive
 341 dust and biomass burning, including road dust, industrial dust, and soil dust. Factor 6 (Fig. 3f) was unidentified and could be
 342 affected by coal combustion, industrial processes, and biomass burning. In the absence of a clear designation of the source,
 343 Factor 6 was attributed to an erroneous contribution from a different source.

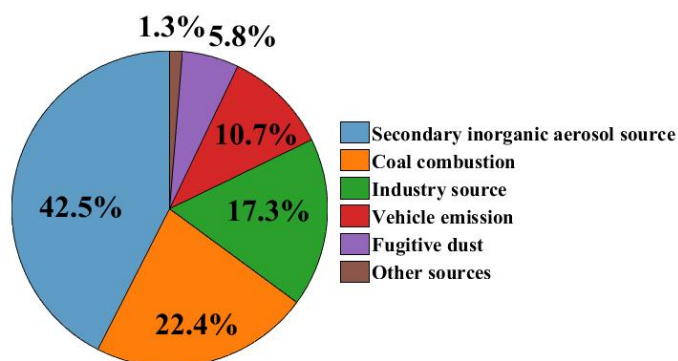


344
 345 **Figure 3. Factor profile in each source for $\text{PM}_{2.5}$ during the whole year. The histograms are the mass concentration of each species**
 346 **to every species ($\mu\text{g}\cdot\text{m}^{-3}$), and the red dots are the relative contributions of each source to every species (%).**
 347

348 Table 3 and Figure 4 show the comparisons of our PMF results with the previous findings. In the YED region, SIS
 349 contributed about 42.5% to PM_{2.5} in Nanjing in this study, which was higher than that reported by Li et al. (2020), while the
 350 contributions of CC was lower. However, other sources of PM_{2.5} in different cities were more complicated. In the BTH, IS
 351 was crucial source and contributed about 30% of Tianjin and Shijiazhuang (Huang et al., 2017). In contrast, IS in Nanjing
 352 contributed only 17.3% of PM_{2.5} pollution. Recent emission control policies in the YRD have had positive effects on
 353 reducing industrial pollution. In the PRD, vehicle emissions, secondary nitrate, coal burning, and industrial emissions
 354 showed obvious local emission characteristics. An extra 30% PM_{2.5} concentration was tightly related to local emissions in
 355 the downtown and industrial areas (Huang et al., 2014; Li et al., 2020; Chow et al., 2022). In this study, VE contributed only
 356 10.7% in Nanjing. It is worth noting that the PMF model assumes that source profiles do not change significantly over time
 357 and that species do not undergo chemical reactions (Paatero and Tapper, 1994). The human activities under seasonal
 358 variations in this study made the actual pollution incompatible with the ideal assumption. For example, emissions from coal
 359 combustion increased the contribution of CC in winter significantly (Xu et al., 2021). In addition, the sources of air masses
 360 in each season also created uncertainties. All of these required detailed discussions of regional transport conditions in each
 361 season.

362 **Table 3. Comparisons of source apportionment among different cities.**

Location		Time	Main pollution sources (proportion)	Investigator
YRD	Nanjing	2018	SIS (42.5%); CC (22.4%); IS (17.3%); VE (10.7%); FD (5.8%)	This study
	Nanjing	2015	SIS (31.5%); CC (27.3%); Road dust (26.5%); Oil combustion (8.5%); IS (5.1%)	Li et al. (2020)
	Ningbo	2015	SIS (39.2%); VE (21.4%); CC (12.4%); IS (9.5%); Ship emission (7.4%); BB (5.1); Aged sea salt (3.7%)	Li et al. (2018)
BTH	Beijing	2017	SIS (35.6%); CC (30.8%); BB (17.6%); VE (12.4%); IS (6.3%)	Xu et al. (2021)
	Tianjin	2014	SIS (29.2%); IS (28.2%); CC (12.4%); VE (11.7%); Dust (11.7%); BB (5.3%)	Huang et al. (2017)
	Shijiazhuang	2014	SIS (36.4%); IS (27.3%); CC (15.5%); VE (8.5%); Dust (7.0%); BB (2.8%)	Huang et al. (2017)
PRD	Hong Kong	2015	SIS (44.9%); IS (13.5%); BB (10.8%); VE (8.6%); Oil combustion (5.3%); Aged sea salt (2.1%)	Chow et al. (2022)
	Shenzhen	2014	SIS (39.3%); VE (26.9%); BB (9.8%); Aged sea salt (4.7%); Dust (3.5)	Huang et al. (2014)
	Guangzhou	2014	SIS (34.6%); VE (28.6%); BB (23.1%); CC (17.7%); Ship emission (14.0%); IS (4.7%)	Li et al. (2020)



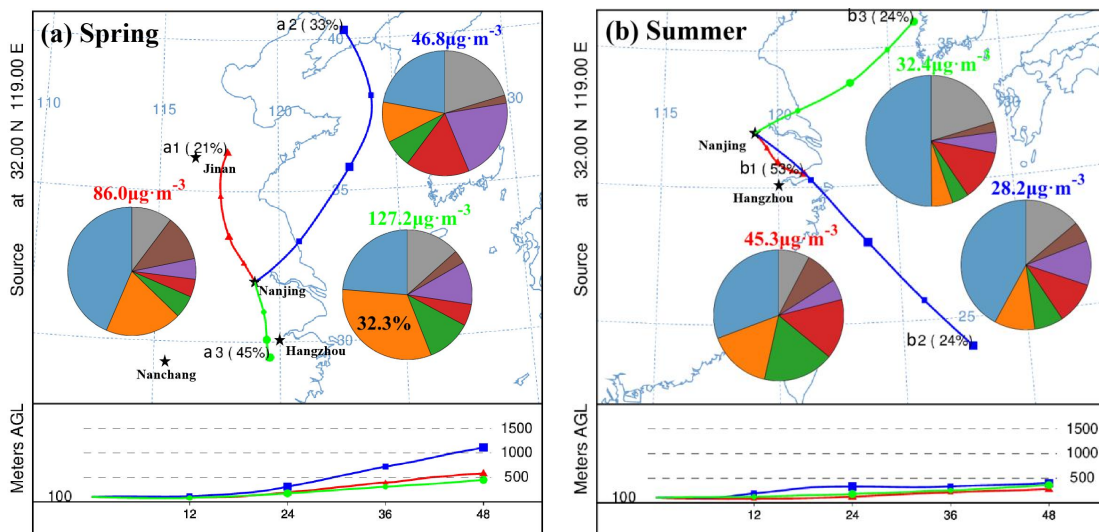
363
 364 **Figure 4. Average annual contribution of the sources identified for PM_{2.5} in Nanjing in 2018.**
 365

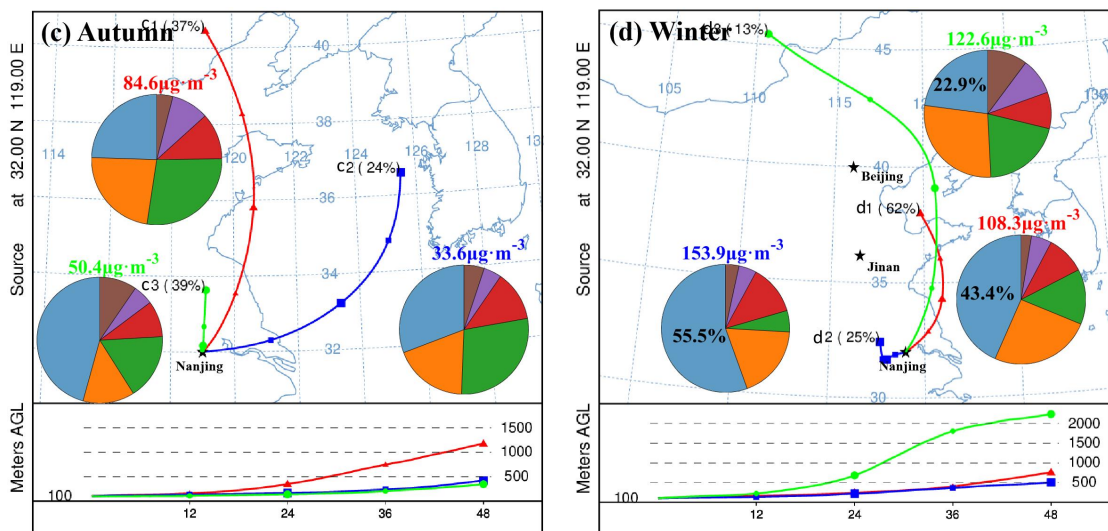
366 **3.3.2 Source identification by backward air mass trajectory analysis**

367 The regional transport of air pollutants exerts a profound impact on local air quality (Shu et al., 2017). Figure 5 shows
 368 the quantified contributions of PM_{2.5} with 48-h backward trajectories. In spring (Fig 5a), nearly half of the air masses (cluster
 369 a3) stemmed from northern Jiangxi, passed over Anhui Province before arriving at the sampling sites, and had the highest
 370 PM_{2.5} average value (127.2 $\mu\text{g}\cdot\text{m}^{-3}$). CC from cluster a3 had the highest contribution with mass and percentage contributions
 371 being 41.0 $\mu\text{g}\cdot\text{m}^{-3}$ and 32.3%, respectively. In addition, FD contributed relatively highly in clusters a2 and a3, with
 372 proportions of 18.2% and 10.3%, respectively. Increased contribution from fugitive dust was related to industrial and
 373 construction activities (Xu et al., 2016). Cluster a2 originated in Liaoning and Cluster a3 was from northern Jiangxi. There
 374 were many industrial cities located in Liaoning, and the largest coal-fired thermal power plant in Jiangxi was located in the
 375 northern city of Jiujiang (Xu et al., 2016; Wang et al., 2019). Long-range transport of dust from these areas would have a
 376 high impact on the formation of severe particle pollution in the YRD. In summer (Fig 5b), the most obvious characteristic of
 377 regional transport was significantly influenced by the ocean. Clusters b2 and b3 were relatively clean with low
 378 concentrations of PM_{2.5} (28.2 $\mu\text{g}\cdot\text{m}^{-3}$ for b2 and 32.4 $\mu\text{g}\cdot\text{m}^{-3}$ for b3). These clusters passed over the ocean areas and
 379 accounted for more than half of all trajectories. The magnitude of total CC, IS and VE exhibited a descending order from
 380 clusters b1 to b3. The dilution effects of clean ocean air masses played a vital role in particulate pollution. In autumn (Fig
 381 5c), there were the highest concentrations of PM_{2.5} in cluster c1, with an average value of 84.6 $\mu\text{g}\cdot\text{m}^{-3}$. CC (23.1%) and IS
 382 (27.6%) contributed relatively highly in cluster c1, indicating that regional transport from industrial regions might play an
 383 important role. For SIS, the proportion of NH₄⁺ in these air masses was significantly higher in autumn than those in other
 384 seasons (Table 2). The increase in the proportion of NH₄⁺ indicated that air pollution masses were heavily affected by nearby
 385 agricultural activities. In winter (Fig 5d), clusters d1 (108.3 $\mu\text{g}\cdot\text{m}^{-3}$) and d3 (122.6 $\mu\text{g}\cdot\text{m}^{-3}$) originated from Shandong
 386 Province and the BTH, accounting for more than three-quarters of the air masses. These air masses, which moved at high
 387 altitudes with a slow speed, could have carried abundant air pollutants. Cluster d2 (153.9 $\mu\text{g}\cdot\text{m}^{-3}$) was short-distance
 388 transport and derived from Jiangsu Province. The contribution of SIS exhibited a increasing order from clusters d1 (22.9%)

389 to d3 (43.4%) to d2 (55.5%), corresponding to the transition from long-range transport air masses to short-distance transport
 390 air masses.

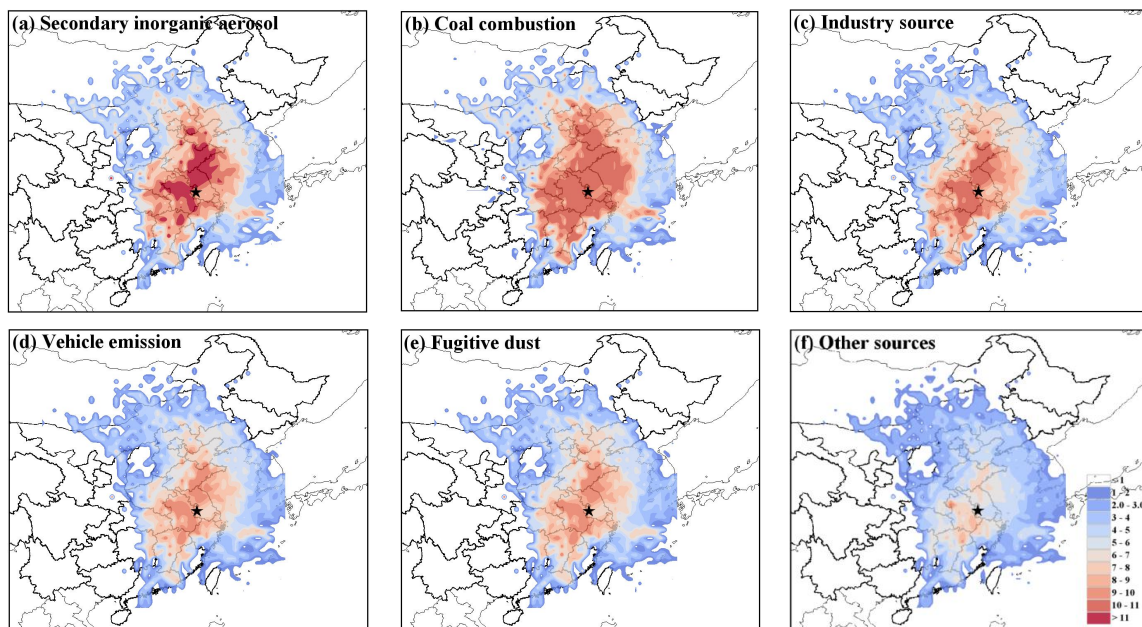
391 Figure 6 shows the spatial distribution of the contribution from each source of PM_{2.5} by the CWT method and
 392 highlighted the potential geographic origins. For SIS (Fig. 6a), the high levels (10-15 $\mu\text{g}\cdot\text{m}^{-3}$) of this source mainly
 393 originated from local emissions in Jiangsu and regional transport from Shandong Province. For CC (Fig. 6b), the high
 394 emissions (10-11 $\mu\text{g}\cdot\text{m}^{-3}$) were distributed in the YRD and central China. The weighted concentration values of CC were
 395 lower than those of the SIS. High concentrations near the center area are associated with local sources, while those far away
 396 from the center area are indicative of regional transport (Shu et al., 2017). The secondary aerosol source was probably from
 397 the accumulation of precursors emitted by local emissions. For IS and VE (Fig. 6c and d), there were no high potential areas
 398 for these sources. The moderate weighted concentration values of IS (8-10 $\mu\text{g}\cdot\text{m}^{-3}$) were potentially located in the north of
 399 Jiangsu, Anhui, and Jiangxi, which were the most important industrial base in China. The oceanic air masses are influenced
 400 by tropical cyclones with high temperature and strong wind (Li et al., 2018; Chow et al., 2022). Based on the backward
 401 trajectory calculation, most of the long-range transport of PM_{2.5} passed through the Yellow Sea and the East Sea. High wind
 402 speed had a great effect on mitigating PM_{2.5} pollution.





■ Secondary inorganic aerosol
 ■ Coal combustion
 ■ Industry source
 ■ Vehicle emission
 ■ Fugitive dust
 ■ Other sources

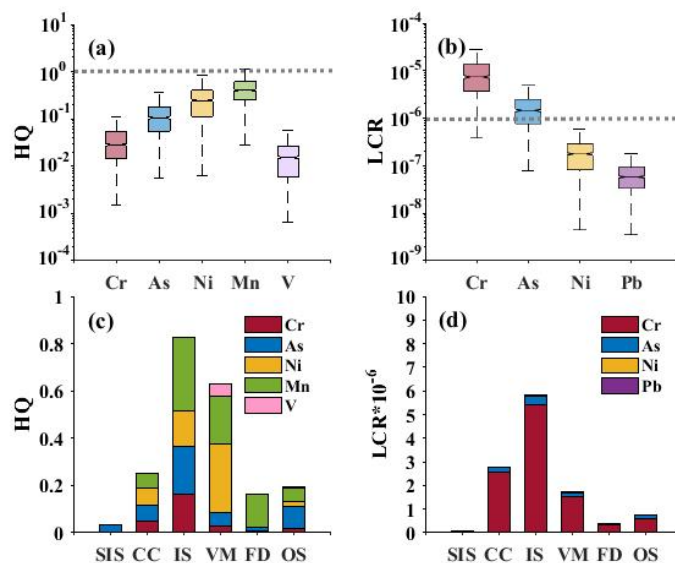
403
 404 **Figure 5. Source contributions to PM_{2.5} grouped by air masses associated with different 48-h backward trajectory clusters. The pie**
 405 **charts show the average source contribution for corresponding clusters.**
 406



407 **Figure 6. Potential source regions for individual sources of PM_{2.5} identified by the CWT method from March 2018 to February**
 408 **2019.**

409
 410 **3.4 Non-carcinogenic and carcinogenic health risks of toxic metal elements in each source of PM_{2.5}**

411 Figure 7 shows the HQ values of non-carcinogenic and the LCR values of carcinogenic risks in PM_{2.5} and their total
 412 health risk in each source. For non-carcinogenic risk (Fig. 7a), the order of the average HQ values was Mn(0.47) > Ni
 413 (0.32) > As (0.14) > Cr (0.04) > V (0.02). The HQ values of toxic elements were all less than one, which indicated that there
 414 was no significant non-carcinogenic risk. However, the summation of five HQ values was higher than one, indicating that
 415 the combined exposure to the pollutant class still had adverse effects. The carcinogenic risk (Fig. 7b) posed by Ni (2.3×10^{-7})
 416 and Pb (6.8×10^{-8}) were lower than 1×10^{-6} and could be acceptable. The carcinogenic risk level of Cr (1.0×10^{-7}) and As
 417 (1.8×10^{-5}) were within the tolerance or acceptable level (1×10^{-6} - 1×10^{-4}) (Zheng et al., 2019). Figures 7 c and d show the
 418 integrated assessment of the source apportionment in toxic elements. IS accounted for the largest proportion of the non-
 419 carcinogenic and carcinogenic risk, with the HQ of 0.83 and the LCR of 5.8×10^{-6} , respectively. Although the PMF results
 420 indicated that SIS had the highest contribution to PM_{2.5} (Fig. 4), the health risk results showed that the health risks of toxic
 421 elements from IS and CC were much higher than those from SIS. Previous studies showed that coal combustion sources in
 422 Beijing, Shanxi, and Jinan had higher respiratory exposure and health risks, while the fugitive dust source in Liaoning
 423 contained higher levels of Pb, As, and Co (Zeng et al., 2019). As, Cr, and Ni in PM_{2.5} were within the acceptable level for
 424 both children and adults in Nanjing, but there was a potential carcinogenic risk posed by Pb via ingestion to children and
 425 adults (Hu et al., 2012). It was related to the differences in PM_{2.5} pollution characteristics and source contributions in
 426 different cities. The ingestion exposure may result in the potential health risk from IS, CC, and VE. Based on the
 427 implementation of energy conservation and emission reduction policies, the main source of pollution in Nanjing is SIS at
 428 present, and the health risk has been alleviated. However, we should pay more attention to the health burden of vehicle
 429 emissions, coal combustion, and industrial processes.



430
 431 **Figure 7. Non-carcinogenic (a) and carcinogenic (b) risks of toxic elements. Non-carcinogenic (c) and carcinogenic (d) risk of the**
 432 **sources identified for PM_{2.5} in Nanjing.**

433 3. Conclusions

434 Identifying and quantitatively assessing the contributions and health risks of pollution sources has played an important
435 role in formulating policies to control particle pollution. We have derived a high-quality PM_{2.5} composition data set, based
436 on a chemical component monitoring from March 2018 to February 2019 in Nanjing. The PMF and back-trajectory results
437 were adopted to investigate the chemical characteristics and regional transports of each source. The health risk assessment
438 was used to explore non-carcinogenic and carcinogenic risks of toxic elements.

439 The results showed that PM_{2.5} concentrations ranged from 6.7 to 234.0 $\mu\text{g}\cdot\text{m}^{-3}$, with an annual average of 68.7 $\mu\text{g}\cdot\text{m}^{-3}$.
440 Water-soluble ions contributed the most to PM_{2.5}. From summer to winter, the $\text{NO}_3^-/\text{SO}_4^{2-}$ ratio increased from 1.2 to 1.59.
441 OC/EC ratio decreased by 56.1% from clean days to heavy pollution days. The average OC/EC ratio on heavy pollution days
442 was 1.3. Both the increase in motor vehicle emissions and the formation of meteorological conditions conducive to pollutant
443 accumulation contribute to the decrease in the OC/EC ratio. Based on the PMF model, the source variations and health risks
444 were assessed. The contribution of identified sources (including SIS (42.5%), CC (22.4%), IS (17.3%), VE (10.7%), FD
445 (5.8%), and other sources (1.3%)) had different spatial distributions and seasonal variations. The CWT analysis indicated
446 that high emissions (10-11 $\mu\text{g}\cdot\text{m}^{-3}$) of SIS and CC were distributed in the YRD and central China in winter. Moderate
447 emissions (8-9 $\mu\text{g}\cdot\text{m}^{-3}$) of IS and VE were potentially located in the north of Jiangsu, Anhui, and Jiangxi. The carcinogenic
448 and non-carcinogenic risks of toxic elements (Cr, As, Ni, Mn, V, and Pb) mainly came from IS, VE, and CC, which were
449 within the tolerance or acceptable level. Based on the implementation of energy conservation and emission reduction
450 policies, the main source of pollution in Nanjing is SIS at present, and the health risk has been alleviated. However, we
451 should pay more attention to the health burden of vehicle emissions, coal combustion, and industrial processes.

452 This study provided new insight for PM_{2.5} research between the source apportionment and health risk. The results
453 presented characteristics of chemical components, pinpointed secondary transformation processes leading to the high PM_{2.5}
454 concentrations, revealed spatial variations of source contribution, and provided new references for mega-cities to conduct
455 health risk analysis on air pollution control measures.

456

457 ***Data Availability.***

458 PM_{2.5} composition data were collected by the atmospheric heavy metal Monitor and the In-situ Gas and Aerosol
459 Compositions Monitor in the School of Atmospheric Sciences, Nanjing University. Air quality monitoring data were
460 acquired from the official NEMC real-time publishing platform (<https://air.cnemc.cn:18007/>, last access: 7 April 2023).
461 Meteorological data were obtained from the University of Wyoming website (<http://weather.uwyo.edu/>, last access: 7 April
462 2023). The NCEP FNL data were taken from the NCEP (<https://rda.ucar.edu/datasets/>, last access: 7 April 2023). These data
463 can be downloaded for free as long as one agrees to the official instructions.

464

465 ***Author contributions.***

466 YZ and MX had original ideas, designed the research, collected the data, and prepared the original draft. YZ, WZ, YL, and
467 RZ performed PMF experiments and carried out the data analysis. MX and WZ acquired financial support for the project
468 leading to this publication. GD, TW, SL, BZ, and ML reviewed the initial draft and checked the English of the original paper.
469

470 ***Acknowledgments.***

471 The authors are grateful to NEMC for the air quality monitoring data, to NCDC for the meteorological data, and to NCEP for
472 global final analysis fields. We gratefully acknowledge the NOAA Air Resources Laboratory (ARL) for providing the
473 HYSPLIT transport and dispersion model used in this work. We acknowledge the Chinese Academy of Meteorological
474 Sciences for supporting this work (<http://www.meteothink.org/>, last access: 7 April 2023).
475

476 ***Competing interests.***

477 The contact author has declared that neither they nor their co-author has any competing interests.
478

479 ***Financial support.***

480 This research has been supported by the Natural Science Foundation of Jiangsu Province (grant no. BK20211158), the
481 National Nature Science Foundation of China (grant no. 42275102), and the Basic Special Business Fund for R&D for the
482 Central Level Scientific Research Institutes of Nanjing Institute of Environmental Sciences (grant no. GYZX210501)

483 **References**

484 Behrooz, R. D., Kaskaoutis, D. G., Grivas, G., and Mihalopoulos, N.: Human health risk assessment for toxic elements in the
485 extreme ambient dust conditions observed in Sistan, Iran, *Chemosphere*, 262,
486 <https://doi.org/10.1016/j.chemosphere.2020.127835>, 2021.

487 Brokamp, C., Jandarov, R., Rao, M. B., LeMasters, G., and Ryan, P.: Exposure assessment models for elemental components
488 of particulate matter in an urban environment: A comparison of regression and random forest approaches, *Atmos.*
489 *Environ.*, 151, 1-11, <https://doi.org/10.1016/j.atmosenv.2016.11.066>, 2017.

490 Chen, D., Cui, H. F., Zhao, Y., Yin, L. N., Lu, Y., and Wang, Q. G.: A two-year study of carbonaceous aerosols in ambient
491 PM_{2.5} at a regional background site for western Yangtze River Delta, China, *Atmos. Res.*, 183, 351-361,
492 <https://doi.org/10.1016/j.atmosres.2016.09.004>, 2017.

493 Chen, Z. Y., Xie, X. M., Cai, J., Chen, D. L., Gao, B. B., He, B., Cheng, N. L., and Xu, B.: Understanding meteorological
494 influences on PM_{2.5} concentrations across China: a temporal and spatial perspective, *Atmos. Chem. Phys.*, 18, 5343-5358,
495 <https://doi.org/10.5194/acp-18-5343-2018>, 2018.

496 Cheng, J., Tong, D., Zhang, Q., Liu, Y., Lei, Y., Yan, G., Yan, L., Yu, S., Cui, Y. R., Clarke, L., Geng, G. G., Zheng, B.,
497 Zhang, X. T., Davis, S. J., He, K. B.: Pathways of China's PM_{2.5} air quality 2015–2060 in the context of carbon neutrality.
498 *National Science Review*, 8(12), nwab078, <https://doi.org/10.1093/nsr/nwab078>, 2021.

499 Chow, W. S., Huang, X. H. H., Leung, K. F., Huang, L., Wu, X. R., and Yu, J. Z.: Molecular and elemental marker-based
500 source apportionment of fine particulate matter at six sites in Hong Kong, China, *Sci. Total Environ.*, 813,
501 <https://doi.org/10.1016/j.scitotenv.2021.152652>, 2022.

502 Conibear, L., Butt, E. W., Knote, C., Arnold, S. R., and Spracklen, D. V.: Residential energy use emissions dominate health
503 impacts from exposure to ambient particulate matter in India. *Nature communications*, 9(1), 617,
504 <https://doi.org/10.1038/s41467-018-02986-7>, 2018.

505 Fan, H., Zhao, C. F., and Yang, Y. K.: A comprehensive analysis of the spatio-temporal variation of urban air pollution in
506 China during 2014–2018, *Atmos. Environ.*, 220, <https://doi.org/10.1016/j.atmosenv.2019.117066>, 2020.

507 Fang, B., Zeng, H., Zhang, L., Wang, H. W., Liu, J. J., Hao, K. L., Zheng, G. Y., Wang, M. M., Wang, Q., and Yang, W. Q.:
508 Toxic metals in outdoor/indoor airborne PM_{2.5} in port city of Northern, China: Characteristics, sources, and personal
509 exposure risk assessment, *Environ. Pollut.*, 279, <https://doi.org/10.1016/j.envpol.2021.116937>, 2021.

510 Feng, X. Y., Tian, Y. Z., Xue, Q. Q., Song, D. L., Huang, F. X., and Feng, Y. C.: Measurement report: Spatiotemporal and
511 policy-related variations of PM_{2.5} composition and sources during 2015–2019 at multiple sites in a Chinese megacity,
512 *Atmos. Chem. Phys.*, 21, 16219–16235, <https://doi.org/10.5194/acp-21-16219-2021>, 2021.

513 Gao, D., Xie, M., Liu, J., Wang, T. J., Ma, C. Q., Bai, H. K., Chen, X., Li, M. M., Zhuang, B. L., and Li, S.: Ozone
514 variability induced by synoptic weather patterns in warm seasons of 2014–2018 over the Yangtze River Delta region,
515 *China, Atmos. Chem. Phys.*, 21, 5847–5864, <https://doi.org/10.5194/acp-21-5847-2021>, 2021.

516 Gao, J. J., Wang, K., Wang, Y., Liu, S. H., Zhu, C. Y., Hao, J. M., Liu, H. J., Hua, S. B., Tian, H. Z.: Temporal-spatial
517 characteristics and source apportionment of PM_{2.5} as well as its associated chemical species in the Beijing-Tianjin-Hebei
518 region of China, *Environ. Pollut.*, 233, 714–724, <https://doi.org/10.1016/j.envpol.2017.10.123>, 2018.

519 Guevara, M., Jorba, O., Soret, A., Petetin, H., Bowdalo, D., Serradell, K., Tena, C., van der Gon, H. D., Kuenen, J., Peuch, V.
520 H., and Garcia-Pando, C. P.: Time-resolved emission reductions for atmospheric chemistry modelling in Europe during
521 the COVID-19 lockdowns, *Atmos. Chem. Phys.*, 21, 773–797, <https://doi.org/10.5194/acp-21-773-2021>, 2021.

522 Hayes, R. B., Lim, C., Zhang, Y., Cromar, K., Shao, Y., Reynolds, H. R., Silverman, D. T., Jones, R. R., Park, Y., Jerrett, M.,
523 Ahn, J., and Thurston, G. D.: PM_{2.5} air pollution and cause-specific cardiovascular disease mortality. *International journal*
524 *of epidemiology*, 49(1), 25–35, <https://doi.org/10.1093/ije/dyz114>, 2019.

525 Hu, X., Zhang, Y., Ding, Z. H., Wang, T. J., Lian, H. Z., Sun, Y. Y., and Wu, J. C.: Bioaccessibility and health risk of
526 arsenic and heavy metals (Cd, Co, Cr, Cu, Ni, Pb, Zn and Mn) in TSP and PM_{2.5} in Nanjing, China, *Atmos. Environ.*, 57,
527 146–152, <https://doi.org/10.1016/j.atmosenv.2012.04.056>, 2012.

528 Huang, X. F., Yun, H., Gong, Z. H., Li, X., He, L. Y., Zhang, Y. H., and Hu, M.: Source apportionment and secondary
529 organic aerosol estimation of PM_{2.5} in an urban atmosphere in China. *Sci. China Earth Sci.* 57, 1352–1362 (2014).
530 <https://doi.org/10.1007/s11430-013-4686-2>, 2014.

531 Huang, X. J., Liu, Z. R., Liu, J. Y., Hu, B., Wen, T. X., Tang, G. Q., Zhang, J. K., Wu, F. K., Ji, D. S., Wang, L. L., and
532 Wang, Y. S.: Chemical characterization and source identification of PM_{2.5} at multiple sites in the Beijing-Tianjin-Hebei
533 region, China, *Atmos. Chem. Phys.*, 17, 12941-12962, <https://doi.org/10.5194/acp-17-12941-2017>, 2017.

534 Islam, M. R., Jayarathne, T., Simpson, I. J., Werden, B., Maben, J., Gilbert, A., Praveen, P. S., Adhikari, S., Panday, A. K.,
535 Rupakheti, M., Blake, D. R., Yokelson, R. J., DeCarlo, P. F., Keene, W. C., and Stone, E. A.: Ambient air quality in the
536 Kathmandu Valley, Nepal, during the pre-monsoon: concentrations and sources of particulate matter and trace gases,
537 *Atmos. Chem. Phys.*, 20, 2927-2951, <https://doi.org/10.5194/acp-20-2927-2020>, 2020.

538 Jeong, C. H., Wang, J. M., Hilker, N., Debosz, J., Sofowote, U., Su, Y., Noble, M., Healy, R., Munoz, T., Celo, V., White, L.,
539 Audette, C., Herod, D., and Evans, G. J.: Temporal and spatial variability of traffic-related PM_{2.5} sources: Comparison of
540 exhaust and non-exhaust emissions, *Atmos. Environ.*, 198, 55-69. <https://doi.org/10.1016/j.atmosenv.2018.10.038>, 2019.

541 Jiang, N., Duan, S. G., Yu, X., Zhang, R. Q., and Wang, K.: Comparative major components and health risks of toxic
542 elements and polycyclic aromatic hydrocarbons of PM_{2.5} in winter and summer in Zhengzhou: Based on three-year data,
543 *Atmos. Res.*, 213, 173-184, <https://doi.org/10.1016/j.atmosres.2018.06.008>, 2018.

544 Khan, M. F., Latif, M. T., Saw, W. H., Amil, N., Nadzir, M. S. M., Sahani, M., Tahir, N. M., and Chung, J. X.: Fine
545 particulate matter in the tropical environment: monsoonal effects, source apportionment, and health risk assessment,
546 *Atmos. Chem. Phys.*, 16, 597-617, <https://doi.org/10.5194/acp-16-597-2016>, 2016.

547 Kumari, P., and Toshniwal, D.: Impact of lockdown measures during COVID-19 on air quality- A case study of India, *Int. J.*
548 *Environ. Health Res.*, 32, 503-510, <https://doi.org/10.1080/09603123.2020.1778646>, 2022.

549 Li, M., Hu, M., Guo, Q., Tan, T., Du, B., Huang, X., He, L., Guo, S., Wang, W., Fan, Y. and Xu, D.: Seasonal Source
550 Apportionment of PM_{2.5} in Ningbo, a Coastal City in Southeast China, *Aerosol Air Qual. Res.*, 18: 2741-2752.
551 <https://doi.org/10.4209/aaqr.2018.01.0011>, 2018.

552 Li, S. W., Chang, M. H., Li, H. M., Cui, X. Y., and Ma, L. Q.: Chemical compositions and source apportionment of PM_{2.5}
553 during clear and hazy days: Seasonal changes and impacts of Youth Olympic Games. *Chem.*, 256, 127163,
554 <https://doi.org/10.1016/j.chemosphere.2020.127163>, 2020.

555 Li, T. T., Li, J., Jiang, H. X., Chen, D. H., Zong, Z., Tian, C. G., and Zhang, G.: Source Apportionment of PM(2.5)in
556 Guangzhou Based on an Approach of Combining Positive Matrix Factorization with the Bayesian Mixing Model and
557 Radiocarbon, *Atmos.*, 11, <https://doi.org/10.3390/atmos11050512>, 2020.

558 Li, X. Y., Cheng, T. H., Shi, S. Y., Guo, H., Wu, Y., Lei, M., Zuo, X., Wang, W. N., and Han, Z. Y.: Evaluating the impacts
559 of burning biomass on regional transport under various emission conditions, *Sci. Total Environ.*, 793,
560 <https://doi.org/10.1016/j.scitotenv.2021.148481>, 2021.

561 Li, X., Yan, C. Q., Wang, C. Y., Ma, J. J., Li, W. X., Liu, J. Y., and Liu, Y.: PM_{2.5}-bound elements in Hebei Province,
562 China: Pollution levels, source apportionment and health risks, *Sci. Total Environ.*, 806,
563 <https://doi.org/10.1016/j.scitotenv.2021.150440>, 2022.

564 Liu, J., Wu, D., Fan, S. J., Mao, X., and Chen, H. Z.: A one-year, on-line, multi-site observational study on water-soluble
565 inorganic ions in PM_{2.5} over the Pearl River Delta region, China, *Sci. Total Environ.*, 601, 1720-1732,
566 <https://doi.org/10.1016/j.scitotenv.2017.06.039>, 2017.

567 Liu, Y. K., Yu, Y. P., Liu, M., Lu, M., Ge, R. R., Li, S. W., Liu, X. R., Dong, W. B., and Qadeer, A.: Characterization and
568 source identification of PM_{2.5}-bound polycyclic aromatic hydrocarbons (PAHs) in different seasons from Shanghai,
569 China, *Sci. Total Environ.*, 644, 725-735, <https://doi.org/10.1016/j.scitotenv.2018.07.049>, 2018.

570 Liu, Z. R., Gao, W. K., Yu, Y. C., Hu, B., Xin, J. Y., Sun, Y., Wang, L. L., Wang, G. H., Bi, X. H., Zhang, G. H., Xu, H. H.,
571 Cong, Z. Y., He, J., Xu, J. S., and Wang, Y. S.: Characteristics of PM_{2.5} mass concentrations and chemical species in
572 urban and background areas of China: Emerging results from the CARE-China network. *Atmos. Chem. Phys.*, 18(12),
573 8849-8871, <https://doi.org/10.5194/acp-18-8849-2018>, 2018.

574 Liu, M. X., Huang, X., Song, Y., Tang, J., Cao, J. J., Zhang, X. Y., Zhang, Q., Wang, S. X., Xu, T. T., Kang, L., Cai, X. H.,
575 Zhang, H. S., Yang, F. M., Wang, H. B., Yu, J. Z., Lau, A. K. H., He, L. Y., Huang, X. F., Duan, L., Ding, A. J., Xue, L.
576 K., Gao, J., Liu, B., and Zhu, T.: Ammonia emission control in China would mitigate haze pollution and nitrogen
577 deposition, but worsen acid rain, *Proc. Natl. Acad. Sci. U. S. A.*, 116, 7760-7765,
578 <https://doi.org/10.1073/pnas.1814880116>, 2019.

579 Liu, L., Zhang, J., Du, R. G., Teng, X. M., Hu, R., Yuan, Q., Tang, S. S., Ren, C. H., Huang, X., Xu, L., Zhang, Y. X.,
580 Zhang, X. Y., Song, C. B., Liu, B., Lu, G. D., Shi, Z. B., and Li, W. J.: Chemistry of atmospheric fine particles during the
581 COVID - 19 pandemic in a megacity of Eastern China. *Geophys. Res.-Atmos.*, 48(2), 2020GL091611,
582 <https://doi.org/10.1029/2020GL091611>, 2020

583 Lv, Z. F., Wang, X. T., Deng, F. Y., Ying, Q., Archibald, A. T., Jones, R. L., Ding, Y., Cheng, Y., Fu, M. L., Liu, Y., Man,
584 H. Y., Xue, Z. G., He, K. B., Hao, J. M., and Liu, H. A.: Source-Receptor Relationship Revealed by the Halted Traffic and
585 Aggravated Haze in Beijing during the COVID-19 Lockdown, *Environ. Sci. Technol.*, 54, 15660-15670,
586 <https://doi.org/10.1021/acs.est.0c04941>, 2020.

587 Lv, L. L., Wei, P., Hu, J. N., Chen, Y. J., and Shi, Y. P.: Source apportionment and regional transport of PM_{2.5} during haze
588 episodes in Beijing combined with multiple models, *Atmos. Res.*, 266, <https://doi.org/10.1016/j.atmosres.2021.105957>,
589 2022.

590 Nie, D. Y., Chen, M. D., Wu, Y., Ge, X. L., Hu, J. L., Zhang, K., and Ge, P. X.: Characterization of Fine Particulate Matter
591 and Associated Health Burden in Nanjing, *Int. J. Env. Res. Public Health*, 15, <https://doi.org/10.3390/ijerph15040602>,
592 2018.

593 Paatero, P., and Tapper, U.: POSITIVE MATRIX FACTORIZATION - A NONNEGATIVE FACTOR MODEL WITH
594 OPTIMAL UTILIZATION OF ERROR-ESTIMATES OF DATA VALUES, *Environmetrics*, 5, 111-126,
595 <https://doi.org/10.1002/env.3170050203>, 1994.

596 Sharma, S., Zhang, M. Y., Anshika, Gao, J. S., Zhang, H. L., and Kota, S. H.: Effect of restricted emissions during COVID-
597 19 on air quality in India, *Sci. Total Environ.*, 728, <https://doi.org/10.1016/j.scitotenv.2020.138878>, 2020.

598 Shu, L., Xie, M., Gao, D., Wang, T. J., Fang, D. X., Liu, Q., Huang, A. N., and Peng, L. W.: Regional severe particle
599 pollution and its association with synoptic weather patterns in the Yangtze River Delta region, China, *Atmos. Chem. Phys.*,
600 17, 12871-12891, <https://doi.org/10.5194/acp-17-12871-2017>, 2017.

601 Silva, L. F., Schneider, I. L., Artaxo, P., Núñez-Blanco, Y., Pinto, D., Flores, É. M., Gómez-Plata, L., Ramírez, O., and
602 Dotto, G. L.: Particulate matter geochemistry of a highly industrialized region in the Caribbean: Basis for future
603 toxicological studies, *Geos. Front*, 13(1), 101-115, <https://doi.org/10.1016/j.gsf.2020.11.012>, 2022.

604 Song, C. B., He, J. J., Wu, L., Jin, T. S., Chen, X., Li, R. P., Ren, P. P., Zhang, L., and Mao, H. J.: Health burden attributable
605 to ambient PM_{2.5} in China. *Environ., Pollut.*, 223, 575-586, <https://doi.org/10.1016/j.envpol.2017.01.060>, 2017.

606 Sulaymon, I. D., Zhang, Y. X., Hopke, P. K., Zhang, Y., Hua, J. X., and Mei, X. D.: COVID-19 pandemic in Wuhan:
607 Ambient air quality and the relationships between criteria air pollutants and meteorological variables before, during, and
608 after lockdown, *Atmos. Res.*, 250, <https://doi.org/10.1016/j.atmosres.2020.105362>, 2021.

609 Tao, J., Zhang, L., Cao, J., and Zhang, R.: A review of current knowledge concerning PM_{2.5} chemical composition, aerosol
610 optical properties and their relationships across China, *Atmos. Chem. Phys.*, 17, 9485–9518, <https://doi.org/10.5194/acp-17-9485-2017>, 2017.

612 Taylor, A. A., Tsuji, J. S., Garry, M. R., McArdle, M. E., Goodfellow, W. L., Adams, W. J., and Menzie, C. A.: Critical
613 Review of Exposure and Effects: Implications for Setting Regulatory Health Criteria for Ingested Copper, *Environ.*
614 *Manage.*, 65, 131-159, <https://doi.org/10.1007/s00267-019-01234-y>, 2020.

615 Thurston, G. D., Burnett, R. T., Turner, M. C., Shi, Y., Krewski, D., Lall, R., Ito, K., Jerrett, M., Gapstur, S. M., Diver, W.
616 R., and Pope III, C. A.: Ischemic heart disease mortality and long-term exposure to source-related components of US fine
617 particle air pollution. *Environ. Health Pers.*, 124(6), 785-794, <https://doi.org/10.1289/ehp.1509777>, 2016.

618 Tong, S. Y., Kong, L. D., Yang, K. J., Shen, J. D., Chen, L., Jin, S. Y., Wang, C., Sha, F., and Wang, L.: Characteristics of
619 air pollution episodes influenced by biomass burning pollution in Shanghai, China, *Atmos. Environ.*, 238,
620 <https://doi.org/10.1016/j.atmosenv.2020.117756>, 2020.

621 Tseng, C. H., Tsuang, B. J., Chiang, C. J., Ku, K. C., Tseng, J. S., Yang, T. Y., Hsu, K. H., Chen, K. C., Yu, S. L., Lee, W.
622 C., Liu, T. W., Chan, C. C., and Chang, G. C.: The Relationship Between Air Pollution and Lung Cancer in Nonsmokers
623 in Taiwan, *J. Thorac. Oncol.*, 14, 784-792, <https://doi.org/10.1016/j.jtho.2018.12.033>, 2019.

624 Veld, M., Alastuey, A., Pandolfi, M., Amato, F., Perez, N., Reche, C., and Querol, X.: Compositional changes of PM_{2.5} in
625 NE Spain during 2009–2018: A trend analysis of the chemical composition and source apportionment, *Sci. Total Environ.*,
626 795, 148728, <https://doi.org/10.1016/j.scitotenv.2021.148728>, 2021.

627 Wang, S. S., Hu, G. R., Yan, Y., Wang, S., Yu, R. L., and Cui, J. Y.: Source apportionment of metal elements in PM_{2.5} in a
628 coastal city in Southeast China: Combined Pb-Sr-Nd isotopes with PMF method, *Atmos. Environ.*, 198, 302-312,
629 <https://doi.org/10.1016/j.atmosenv.2018.10.056>, 2019.

630 Wang, S. B., Ji, Y. Q., Zhao, J. B., Lin, Y., and Lin, Z.: Source apportionment and toxicity assessment of PM_{2.5}-bound PAHs
631 in a typical iron-steel industry city in northeast China by PMF-ILCR, *Sci. Total Environ.*, 713,
632 <https://doi.org/10.1016/j.scitotenv.2019.136428>, 2020.

633 Wang, J. F., Li, J. Y., Ye, J. H., et al.: Fast sulfate formation from oxidation of SO₂ by NO₂ and HONO observed in Beijing
634 haze. *Nat. Commun.*, 11(1), 2844, <https://doi.org/10.1038/s41467-020-16683-x>, 2020.

635 Wang, H. L., Ke, Y., Tan, T., Zhu, B., Zhao, L. T., Yin, Y.: Observational evidence for the dual roles of BC in the megacity
636 of eastern China: Enhanced O₃ and decreased PM_{2.5} pollution, *Chemosphere*, 327,
637 <https://doi.org/10.1016/j.chemosphere.2023.138548>, 2023.

638 Win, M. S., Zeng, J. Y., Yao, C. H., Zhao, M. F., Xiu, G. L., Xie, T. T., Rao, L. F., Zhang, L. Y., Lu, H., Liu, X. C., Wang,
639 Q. Y., and Lu, S. N.: Sources of HULIS-C and its relationships with trace metals, ionic species in PM_{2.5} in suburban
640 Shanghai during haze and non-haze days, *JATC*, 77, 63-81, <https://doi.org/10.1007/s10874-020-09404-7>, 2020.

641 Wong, Y. K., Liu, K. M., Yeung, C., Leung, K. K. M., and Yu, J. Z.: Measurement report: Characterization and source
642 apportionment of coarse particulate matter in Hong Kong: insights into the constituents of unidentified mass and source
643 origins in a coastal city in southern China, *Atmos. Chem. Phys.*, 22, 5017-5031, <https://doi.org/10.5194/acp-22-5017-2022>,
644 2022.

645 Wu, X., Cao, F., Haque, M., Fan, M. Y., Zhang, S. C., and Zhang, Y. L.: Molecular composition and source apportionment
646 of fine organic aerosols in Northeast China, *Atmos. Environ.*, 239, <https://doi.org/10.1016/j.atmosenv.2020.117722>, 2020.

647 Xie, M., Liao, J. B., Wang, T. J., Zhu, K. G., Zhuang, B. L., Han, Y., Li, M. M., and Li, S.: Modeling of the anthropogenic
648 heat flux and its effect on regional meteorology and air quality over the Yangtze River Delta region, China, *Atmos. Chem.*
649 *Phys.*, 16, 6071-6089, <https://doi.org/10.5194/acp-16-6071-2016>, 2016.

650 Xie, J. J., Yuan, C. G., Xie, J., Niu, X. D., and He, A. E.: PM_{2.5}-bound potentially toxic elements (PTEs) fractions,
651 bioavailability and health risks before and after coal limiting, *Ecotoxicol. Environ. Saf.*, 192,
652 <https://doi.org/10.1016/j.ecoenv.2020.110249>, 2020.

653 Xu, H. M., Cao, J. J., Chow, J. C., Huang, R. J., Shen, Z., Chen, L. A., Ho, K. F. and Watson, J. G.: Inter-annual variability
654 of wintertime PM_{2.5} chemical composition in Xi'an, China: evidences of changing source emissions, *Sci. Total Environ.*,
655 545, 546-555, <https://doi.org/10.1016/j.scitotenv.2015.12.070>, 2016.

656 Xu, J. S., Liu, D., Wu, X. F., Vu, T., Zhang, Y. L., Fu, P. Q., Sun, Y. L., Xu, W. Q., Zheng, B., Harrison, R. M., and Shi, Z.
657 B.: Source apportionment of fine organic carbon at an urban site of Beijing using a chemical mass balance model, *Atmos.*
658 *Chem. Phys.*, 21, 7321-7341, <https://doi.org/10.5194/acp-21-7321-2021>, 2021.

659 Yan, Y., Zheng, Q., Yu, R. L., Hu, G. R., Huang, H. B., Lin, C. Q., Cui, J. Y., and Yan, Y.: Characteristics and provenance
660 implications of rare earth elements and Sr-Nd isotopes in PM_{2.5} aerosols and PM_{2.5} fugitive dusts from an inland city of
661 southeastern China, *Atmos. Environ.*, 220, <https://doi.org/10.1016/j.atmosenv.2019.117069>, 2020.

662 Yan, Y. C., Liu, Z. R., Gao, W., Li, J. Y., Zhang, X. H., Chai, W. H., Bai, J. H., Hu, B., and Wang, Y. S.: Physiochemistry
663 characteristics and sources of submicron aerosols at the background area of North China Plain: Implication of air pollution
664 control in heating season, *Atmos. Res.*, 249, <https://doi.org/10.1016/j.atmosres.2020.105291>, 2021.

665 Zeng, Y. Y., Cao, Y. F., Qiao, X., Seyler, B. C., and Tang, Y.: Air pollution reduction in China: Recent success but great
666 challenge for the future, *Sci. Total Environ.*, 663, 329-337, <https://doi.org/10.1016/j.scitotenv.2019.01.262>, 2019.

667 Zhan, Y. Z. H., Xie, M., Gao, D., Wang, T. J., Zhang, M., and An, F. X.: Characterization and source analysis of water-
668 soluble inorganic ionic species in PM_{2.5} during a wintertime particle pollution episode in Nanjing, China, *Atmos. Res.*,
669 262, <https://doi.org/10.1016/j.atmosres.2021.105769>, 2021.

670 Zhang, L. L., Wilson, J. P., MacDonald, B., Zhang, W. H., and Yu, T.: The changing PM_{2.5} dynamics of global megacities
671 based on long-term remotely sensed observations, *Environ. Int.*, 142, <https://doi.org/10.1016/j.envint.2020.105862>, 2020.

672 Zhang, Z. Z., Wang, W. X., Cheng, M. M., Liu, S. J., Xu, J., He, Y. J., and Meng, F.: The contribution of residential coal
673 combustion to PM_{2.5} pollution over China's Beijing-Tianjin-Hebei region in winter, *Atmos. Environ.*, 159, 147-161,
674 <https://doi.org/10.1016/j.atmosenv.2017.03.054>, 2017.

675 Zheng, H., Kong, S. F., Yan, Q., Wu, F. Q., Cheng, Y., Zheng, S. R., Wu, J., Yang, G. W., Zheng, M. M., Tang, L. L., Yin,
676 Y., Chen, K., Zhao, T. L., Liu, D. T., Li, S. L., Qi, S. H., Zhao, D. L., Zhang, T., Ruan, J. J., and Huang, M. Z.: The
677 impacts of pollution control measures on PM_{2.5} reduction: Insights of chemical composition, source variation and health
678 risk, *Atmos. Environ.*, 197, 103-117, <https://doi.org/10.1016/j.atmosenv.2018.10.023>, 2019.

679 Zhou, C. S., Chen, J., and Wang, S. J.: Examining the effects of socioeconomic development on fine particulate matter (PM_{2.}
680 ₅) in China's cities using spatial regression and the geographical detector technique: *Sci. Total Environ.*, 619, 436-445,
681 <https://doi.org/10.1016/j.scitotenv.2017.11.124>, 2018.

682 Zhu, Y. J., Xie, J. G., Huang, F. M., and Cao, L. Q.: Association between short-term exposure to air pollution and COVID-
683 19 infection: Evidence from China, *Sci. Total Environ.*, 727, <https://doi.org/10.1016/j.scitotenv.2020.138704>, 2020.

684 Zong, Z., Wang, X. P., Tian, C. G., Chen, Y. J., Qu, L., Ji, L., Zhi, G. R., Li, J., and Zhang, G.: Source apportionment of
685 PM_{2.5} at a regional background site in North China using PMF linked with radiocarbon analysis: insight into the
686 contribution of biomass burning, *Atmos. Chem. Phys.*, 16, 11249-11265, <https://doi.org/10.5194/acp-16-11249-2016>,
687 2016.

688 Zou, B. B., Huang, X. F., Zhang, B., Dai, J., Zeng, L. W., Feng, N., and He, L. Y.: Source apportionment of PM_{2.5} pollution
689 in an industrial city in southern China, *Atmos. Pollut. Res.*, 8, 1193-1202, <https://doi.org/10.1016/j.apr.2017.05.001>, 2017.

690
691
692